

Shaping Cold Atom Clouds with a Vortex Beam

Arianna Bertoluzza,^{1,*} Sonja Lorenz,¹ Paul Hampp,¹ Moriz Härle,¹ Daniel Braun,¹ David Petrosyan,^{1,2} József Fortágh,¹ and Andreas Günther^{1,†}

¹*Center for Quantum Science, Eberhard Karls Universität Tübingen,
Auf der Morgenstelle 14, 72076 Tübingen, Germany*

²*Institute of Electronic Structure & Laser, FORTH, Heraklion 70013, Crete, Greece*
(Dated: July 8, 2025)

We introduce a method for shaping a cold atom cloud using a vortex laser beam with a polarisation singularity at its center, which creates a point of vanishing intensity. Exploiting this feature we experimentally demonstrate two different schemes to create micron-scaled line- and sheet-like atomic density distributions. In the *dynamic scheme*, atoms in the bright beam regions are accelerated and therefore effectively removed from the cloud. In the *dark-state scheme*, these atoms are pumped into a state that does not interact with the shaping light. In both cases, an atomic distribution remains, either as a thin line or as a sheet when an additional polarizer is used. We find good agreement between the experimental results and our theoretical model, which predicts the method to be in principle not diffraction-limited.

I. INTRODUCTION

Over the last decade, the shaping of cold atom clouds on the micron-scale has become a powerful tool for studying interacting quantum systems [1–4]. To this end, atomic ensembles are typically confined in magnetic or optical traps, which can be engineered to almost arbitrary spatial scales. While macroscopic magnetic confinement can be achieved via conventional coil systems [5], the micron-sized regime is typically accessed in chip-based structures [6–8], with a lower limit in the structure size being given by current constrains and the distance of the cloud to the field generating elements. Optical confinement, on the other hand, allows for a large variety of trapping schemes, ranging from simple single-beam and cross-beam dipole traps [9] to more complex structures, as created in optical lattices [10] or tweezer arrays [11]. Thin atomic distributions and periodic arrangements can then be routinely created [12], laying the foundation for groundbreaking experiments such as studies of Anderson localization [13, 14], topological states [15], or the Mott insulator transition [16]. While such confining potentials have been extensively studied, state-selective shaping of unconfined atom clouds on the micron-scale has not yet been investigated.

Here, we introduce an approach for creating thin line- and sheet-like atomic ensembles based on shaping an atomic cloud via an optical vortex beam with a polarization singularity at the beam center, where the beam intensity vanishes. Then, shining a vortex beam on an atomic cloud allows for selective interaction between the light field and the atoms in the outer beam regions, which can be used to effectively remove (hide) atoms and thus shape the cloud. At lowest order approximation, the intensity profile close to the beam center is parabolic,

with the curvature scaling linearly with the beam power. Therefore, the size of the remaining atomic distribution can be decreased arbitrarily, even below the diffraction limit, by just increasing the beam power, creating a thin line of atoms. Additionally, the inhomogeneous polarization distribution of the vortex beam can be used to create more complex spatial intensity distributions, such as a double-lobed structure featuring a zero-intensity line passing through the center. Then, the resulting beam can be used for the shaping of atomic clouds into sheet-like distributions. In our work, we experimentally demonstrate two different shaping schemes. In the *dynamic scheme*, atoms in bright beam regions are accelerated due to the scattering force from the resonant shaping beam, effectively removing atoms in a selective way across the beam profile. In the *dark-state scheme*, the shaping beam frequency is tuned such that atoms in bright beam regions are instead pumped to a non-interacting dark state, transparent to the shaping beam. In both cases, this leads to the formation of either a micron-scaled line of atoms or, when using an additional polarizer, an atomic sheet. Our experimental results, for a double-lobed beam in the case of the *dynamic scheme* and for a vortex beam in the case of the *dark-state scheme*, show good agreement with the theory, which predicts the method to be in principle not diffraction-limited. Due to the very simple setup and the requirement of low power for the shaping beam, our method makes the generation of micron-scaled, unconfined clouds easily accessible and provides a unique experimental platform for studies with thin atomic ensembles. In particular, this motivates us to employ this technique in future studies of Rydberg interactions in unconfined atomic rubidium ensembles.

The manuscript is structured as follows. Section II provides a theoretical treatment of a cold atom cloud interacting with an optical vortex beam, including the analytic description of a vortex beam with a polarization singularity (II A), the general idea for cloud shaping (II B) and the theoretical description of the *dynamic* (II C) and *dark-state shaping scheme* (II D). The exper-

* arianna.bertoluzza@uni-tuebingen.de

† a.guenther@uni-tuebingen.de

imental setup and the shaping sequence are described in Section III, followed by the individual measurements discussed in Section IV. Here, we present a comparison between experiment and theory for both the *dynamic*- (IV A) and the *dark-state scheme* (IV B).

II. THEORY

A. Vortex Beams

Optical vortex beams feature a point of vanishing intensity at the beam center, caused by the presence of a phase- or polarization singularity. Therefore, appropriate phase- or polarization profiles are imprinted to the beam. Common methods for creating phase singularities make use of spiral phase plates [17], computer-generated holograms [18], spatial light modulators [19] or optical cavities [20], while the generation of polarization singularities requires the use of vortex retarders [21] or q-plates [22]. In principle, the intensity profile of a vortex beam (or any other phase- and/or polarization-modulated beam) can be calculated if the electric field is fully known in a single plane, typically taken to be the plane in which the vortex pattern is generated. In view of the experiments presented in this paper, the following description will focus on a vortex beam with a polarization singularity produced by a vortex retarder, for which we present both a numerical and analytical treatment. However, this analysis can be easily adapted to the case of a phase singularity.

We consider a Gaussian TEM₀₀ beam propagating along the z-axis (cf. Fig. 1), with the beam waist at position $z = 0$, and a vortex retarder with negligible thickness placed in the z' -plane, orthogonal to the beam propagation direction. Without loss of generality, we assume the beam to be linearly polarized along the x-axis and the electric field being described by a two-component Jones vector $\vec{E}(\vec{r}) = (E_x(\vec{r}), E_y(\vec{r}))$ perpendicular to the propagation axis [23]. In cylindrical coordinates $\vec{r} \rightarrow (\rho, \varphi, z)$ and with the input beam polarization $\vec{p}_{\text{in}} = (1, 0)$, the electric field in front of the retarder can then be written as

$$\vec{E}_{\text{in}}(\vec{r}') = E(\vec{r}') \vec{p}_{\text{in}} \quad (1)$$

with

$$E(\vec{r}') = E_0 \frac{w_0}{w(z')} e^{-\frac{\rho'^2}{w(z')^2}} e^{i(kz' + \frac{k\rho'^2}{2R(z')} - \xi(z'))}. \quad (2)$$

Here, $k = 2\pi/\lambda$ is the wavenumber, w_0 the beam waist, $z_0 = \pi w_0^2/\lambda$ the Rayleigh length, $w(z') = w_0 \sqrt{1 + (z'/z_0)^2}$ the beam radius, $R(z') = z'(1 + (z_0/z')^2)$ the wavefront curvature and $\xi(z') = \tan^{-1}(z'/z_0)$ the Gouy phase. The action of a vortex retarder is comparable to that of a half-wave plate for which the angle θ between the fast axis and the horizontal x-axis is a function of the azimuthal angle φ . For a

vortex retarder of order $m \in \mathbb{N}$, we have

$$\theta(\varphi) = \frac{1}{2} m \varphi, \quad (3)$$

with the corresponding Jones-Matrix of a half-wave plate [24]

$$J_{\lambda/2}(\theta) = \begin{pmatrix} \cos 2\theta & \sin 2\theta \\ \sin 2\theta & -\cos 2\theta \end{pmatrix}. \quad (4)$$

The electric field immediately after the plate can then be expressed as

$$\vec{E}_{\text{out}}(\vec{r}') = J_{\lambda/2}(\theta(\varphi')) \vec{E}_{\text{in}}(\vec{r}') = E(\vec{r}') \vec{p}_{\text{out}}(\varphi') \quad (5)$$

with $E(\vec{r}')$ from Eq. (2) and

$$\vec{p}_{\text{out}}(\varphi') = J_{\lambda/2}(\theta(\varphi')) \vec{p}_{\text{in}} = \begin{pmatrix} \cos m\varphi' \\ \sin m\varphi' \end{pmatrix}. \quad (6)$$

The intensity profile of the vortex beam along its propagation direction can be calculated numerically making use of Huygens principle [25], according to which the wavefront of the propagating beam is the result of the interference of secondary spherical wavelets originating from the initial wavefront. The field at position \vec{r} can be expressed as

$$\vec{E}_{\text{out}}(\vec{r}) = -\frac{i}{\lambda} \iint \vec{E}_{\text{out}}(\vec{r}') S(\vec{r} - \vec{r}') dx' dy', \quad (7)$$

which corresponds to the two-dimensional convolution of the original field with the spherical wavelet $S(\vec{r})$

$$S(\vec{r}) = \frac{e^{ikr}}{r} \approx \frac{1}{z} e^{ikz} e^{ik\frac{\rho^2}{2z}}, \quad (8)$$

with $r = |\vec{r}| = \sqrt{\rho^2 + z^2}$ and the Fresnel approximation being used in the limit $\rho \ll z$, at which the wavefronts become parabolic. The overall intensity of the vortex beam is then simply obtained by adding the absolute values squared of the electric field components

$$I_{\text{out}}(\vec{r}) \sim |E_{\text{out},x}(\vec{r})|^2 + |E_{\text{out},y}(\vec{r})|^2, \quad (9)$$

with normalization to the total beam power P

$$\iint I_{\text{out}}(\vec{r}) dx dy = P. \quad (10)$$

Next, we present an analytic description of vortex beams with a polarization singularity, for which two different approaches can be followed. A first and simpler method consists in solving the Helmholtz equation in the paraxial wave approximation using cylindrical coordinates. Assuming a spatially varying polarization, the Vector-Laguerre-Gauss-Modes VLGM_p^m are obtained, with the $p = 0$ solutions featuring a point of zero intensity at the center of the beam due to a polarization singularity. However, these solutions are only valid in the far-field and even there provide only a qualitative description of experimentally generated vortex beams [26]. In

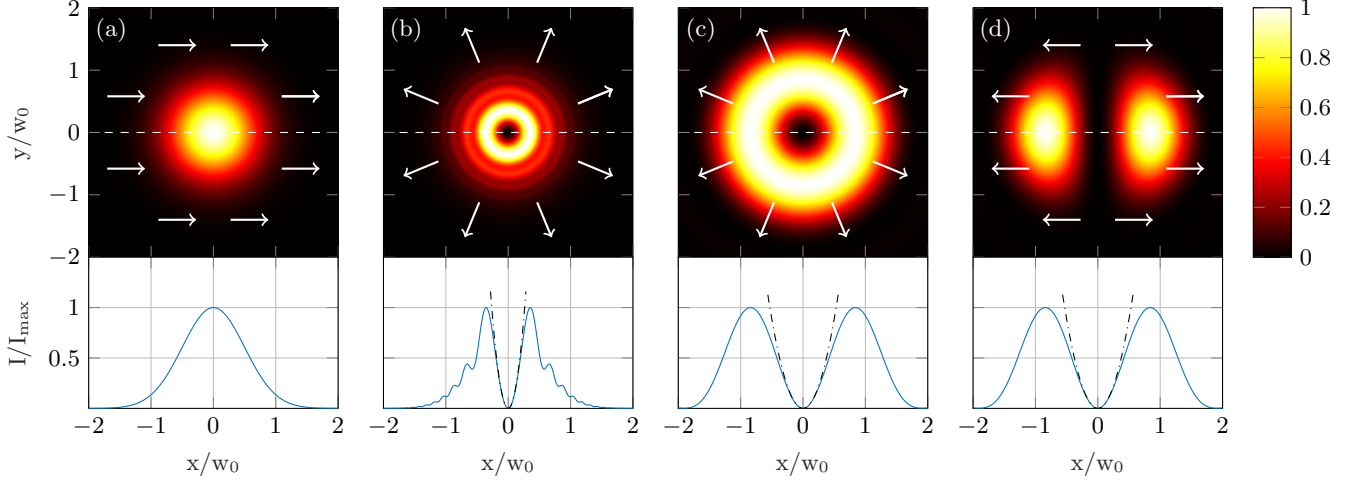


FIG. 1. **Vortex beam.** Intensity profiles of a vortex beam as generated from a Gaussian beam (TEM_{00}) in combination with a $m = 1$ vortex retarder placed at the position of the beam waist ($z' = 0$). Using Eqs. (2), (19) and (23) the profiles are calculated at positions (a) $z = 0$, (b) $z = 0.05 z_0$, (c) $z = 0.5 z_0$, and (d) $z = 0.5 z_0$ with additional polarization filter. The 2D profiles are shown together with 1D line-scans through the beam center ($y = 0$), with the line-scan positions marked in the 2D profiles (white dashed lines). The line-scans in (b)-(d) are extended by parabolic approximations around the beam center (black dash-dotted line) with curvatures calculated from Eq. (22). All intensities are normalized to the maximum intensity and all lengths are normalized to the initial beam waist w_0 . The white arrows in the 2D profiles indicate the direction of the local light field polarization.

the near-field, diffraction effects become visible and an accurate representation can be obtained making use of the Collins-Huygens-Integral [27], which is equivalent to the paraxial Fresnel integral using the ray transfer matrix (also known as ABCD matrix) formalism. Again assuming that the beam propagates along the z -axis, the final electric field distribution at a position z can be calculated for any known initial field at position z' as a function of the ABCD matrix coefficients describing the propagation from z' to z . In cylindrical coordinates,

$$\vec{E}_{\text{out}}(\vec{r}) = -\frac{i}{\lambda B} e^{ik(z-z')} \int_0^\infty \rho' d\rho' \int_0^{2\pi} d\varphi' \vec{E}_{\text{out}}(\vec{r}') \times \exp \left[\frac{ik}{2B} (A\rho^2 + D\rho'^2 - 2\rho\rho' \cos(\varphi - \varphi')) \right], \quad (11)$$

where the propagation matrix for free space evolution is

$$\begin{pmatrix} A & B \\ C & D \end{pmatrix} = \begin{pmatrix} 1 & z - z' \\ 0 & 1 \end{pmatrix}. \quad (12)$$

Then, Eq. (11) follows directly from Eq. (7) for $z > z'$ and using the Fresnel approximation for the spherical wavelet, with $|\vec{r} - \vec{r}'|$ expressed in cylindrical coordinates

$$|\vec{r} - \vec{r}'| \approx (z - z') + \frac{\rho^2 + \rho'^2 - 2\rho\rho' \cos(\varphi - \varphi')}{2(z - z')}. \quad (13)$$

In the following, we will adapt the calculations for the vortex field after a spiral phase plate presented in [28] to the case of a vortex retarder. Inserting Eq. (5) in Eq. (11), we can write the electric field at any position

after the vortex retarder as

$$\vec{E}_{\text{out}}(\vec{r}) = -\frac{i}{\lambda B} E_{00}(\rho, z') e^{ikz} \int_0^\infty \int_0^{2\pi} \begin{pmatrix} \cos m\varphi' \\ \sin m\varphi' \end{pmatrix} \times \exp \left[-\frac{\rho'^2}{R_c(z')^2} \right] \exp \left[-i\frac{\rho'}{\rho_c} \cos(\varphi - \varphi') \right] \rho' d\rho' d\varphi',$$

where we defined

$$E_{00}(\rho, z') = E_0 \frac{w_0}{w(z')} e^{\frac{ikD\rho^2}{2B}} e^{-i\xi(z')} \quad (14a)$$

$$\frac{1}{R_c(z')^2} = \frac{1}{w(z')^2} - \frac{ik}{2R(z')} - \frac{iAk}{2B} \quad (14b)$$

$$\frac{1}{\rho_c} = \frac{k\rho}{B}. \quad (14c)$$

The integral over the azimuthal angle φ' can be solved after substituting $\phi = \varphi - \varphi'$ and using

$$\int_{\varphi-2\pi}^{\varphi} e^{-i(\kappa \cos \phi + m\phi)} d\phi = 2\pi(-i)^{|m|} J_{|m|}(\kappa), \quad (15)$$

with $\kappa = \rho'/\rho_c$ and J_m being the m -th order Bessel function of the first kind. This allows to write

$$\vec{E}_{\text{out}}(\vec{r}) = \frac{(-i)^{|m|+1}}{kB} E_{00}(\rho, z') e^{ikz} \begin{pmatrix} \cos m\varphi \\ \sin m\varphi \end{pmatrix} \times \int_0^\infty \exp \left[-\frac{\rho'^2}{R_c(z')^2} \right] J_{|m|} \left(\frac{\rho'}{\rho_c} \right) \rho' d\rho', \quad (16)$$

where it can be noticed that the propagation does not affect the beam polarization $\vec{p}_{\text{out}} = (\cos(m\varphi'), \sin(m\varphi'))$. This integral can be expressed in terms of a combination of l -th order modified Bessel functions of the first kind \mathcal{I}_l making use of the formula [29]

$$\int_0^\infty x e^{-\epsilon x^2} J_{|m|}(\beta x) dx = \frac{\sqrt{2\pi\eta}}{4\epsilon} e^{-\eta} \left[\mathcal{I}_{\frac{|m|-1}{2}}(\eta) - \mathcal{I}_{\frac{|m|+1}{2}}(\eta) \right],$$

with $\eta = \beta^2/8\epsilon$. Identifying $\epsilon = 1/R_c^2$ and $\beta = 1/\rho_c$ leads to an analytic expression for the electric field of a vortex beam at a position z which is generated by a m -th order vortex retarder placed at z' :

$$\vec{E}_{\text{out}}(\vec{r}) = \frac{2\pi^{3/2}(-i)^{|m|+1} E_{00}(\rho, z') R_c^3(z')}{8\rho_c \lambda B} e^{ikz} \times e^{-\frac{R_c^2}{8\rho_c^2}} \left[\mathcal{I}_{\frac{|m|-1}{2}}\left(\frac{R_c^2}{8\rho_c^2}\right) - \mathcal{I}_{\frac{|m|+1}{2}}\left(\frac{R_c^2}{8\rho_c^2}\right) \right] \vec{p}_{\text{out}}(\varphi). \quad (17)$$

We focus on the case of a vortex beam with $m = 1$, as the one we use later in our experiments. Notice that the field dependence on the azimuthal angle φ is only contained in the polarization vector, allowing to rewrite Eq. (17) as

$$\vec{E}_{\text{out}}(\vec{r}) = \tilde{E}_{\text{out}}(\rho, z) \begin{pmatrix} \cos \varphi \\ \sin \varphi \end{pmatrix}, \quad (18)$$

with

$$\tilde{E}_{\text{out}}(\rho, z) = -\sqrt{\pi} E_0 \frac{w_0}{w(z')} \frac{R_c^3(z') k^2}{8B^2} \rho e^{-\frac{R_c^2(z') k^2}{8B^2} \rho^2} e^{\frac{ikD}{2B} \rho^2} \times \left[\mathcal{I}_0\left(\frac{R_c^2(z') k^2}{8B^2} \rho^2\right) - \mathcal{I}_1\left(\frac{R_c^2(z') k^2}{8B^2} \rho^2\right) \right] e^{i(kz - \xi(z'))}.$$

Then, the intensity profile of the vortex beam can be calculated by taking the absolute value squared of the electric field,

$$I_{\text{out}}(\vec{r}) = |E_{\text{out},x}|^2 + |E_{\text{out},y}|^2 = \left| \tilde{E}_{\text{out}}(\rho, z) \right|^2. \quad (19)$$

Figure 1b and 1c show the calculated 2D profiles at positions $z = 0.05 z_0$ and $z = 0.5 z_0$, respectively, together with 1D line-scans passing through the beam center. Here, the vortex retarder is placed at the beam waist ($z' = 0$). Diffraction fringes are clearly visible in the first case, corresponding to the near-field region, but become less relevant as the plane of observation moves outwards, until they finally disappear. In both cases, an intensity singularity appears at the beam center, which is viewed as point-like in the 2D intensity profiles, but actually corresponds to a line of zero intensity along the beam propagation direction.

With the intention of using a vortex beam to shape an atomic cloud, we now characterize its intensity profile close to the center, which is where the interaction between the vortex beam and the atoms takes place. To this end, we calculate the lowest order Taylor expansion

in ρ of Eq. (19) around the beam center at $\rho = 0$. Knowing that $\mathcal{I}_0(0) = 1$, $\mathcal{I}_1(0) = 0$ and making use of the following expressions for the derivatives of the modified Bessel functions [30]

$$\frac{\partial}{\partial r} \mathcal{I}_0(r) = \mathcal{I}_1(r) \quad (20a)$$

$$\frac{\partial}{\partial r} \mathcal{I}_m(r) = \frac{1}{2} [\mathcal{I}_{m-1}(r) + \mathcal{I}_{m+1}(r)], \quad (20b)$$

one can show that $I_{\text{out}}(\rho = 0) = 0$, $\frac{\partial I_{\text{out}}}{\partial \rho} \Big|_{\rho=0} = 0$, while

$$\begin{aligned} \frac{\partial^2 I_{\text{out}}}{\partial \rho^2} \Big|_{\rho=0} &= 2 \frac{\partial \tilde{E}}{\partial \rho} \left(\frac{\partial \tilde{E}}{\partial \rho} \right)^* \Big|_{\rho=0} \\ &= 2\pi \left| E_0 \frac{w_0}{w(z')} \frac{R_c^3(z') k^2}{8B^2} \right|^2. \end{aligned} \quad (21)$$

We can then approximate the intensity profile of the $m = 1$ vortex beam close to the center with a parabolic function $I \approx \frac{1}{2} \alpha \rho^2$ and find an analytic expression for the radial intensity curvature α

$$\begin{aligned} \alpha &= \frac{\partial^2 I_{\text{out}}}{\partial \rho^2} \Big|_{\rho=0} = \frac{\pi P}{\lambda (z - z') w(z')^2} \\ &\times \left(\left[1 + \frac{z - z'}{z_0} \left(\frac{w_0}{w(z')} \right)^2 \frac{z'}{z_0} \right]^2 + \left[\frac{z - z'}{z_0} \left(\frac{w_0}{w(z')} \right)^2 \right]^2 \right)^{-\frac{3}{2}}, \end{aligned}$$

where we used the ABCD matrix for free-space propagation from z' to z in Eq. (12) and $|E_0|^2 = 2P/\pi w_0^2$ for the Gaussian input beam at the vortex retarder, with P being the beam power. This expression is valid for all z along the beam propagation and the most important thing to notice is that the beam curvature scales linearly with the total power. In the case $z' \ll z_0$, meaning that the vortex retarder is placed well within the Rayleigh length from the waist of the incoming Gaussian beam, a simple expression for α can be obtained

$$\alpha = \frac{\pi}{\lambda (z - z') w_0^2} \left[1 + \frac{z^2 - z'^2}{z_0^2} \right]^{-\frac{3}{2}} P. \quad (22)$$

We note that this result applies for vortex beams generated with both a vortex retarder and with a spiral phase plate of the same order $m = 1$. In fact, their intensity profile is the same regardless of the different type of the central singularity, which is due to the spatially inhomogeneous polarization or phase. In this sense, both beam types could be used effectively to create thin line-like atomic distributions, as explained in section II B. However, beams with a spatially dependent polarization offer an advantage for further beam shaping using e.g. polarization filters. This is illustrated in Fig. 1. This shows how a Gaussian beam with initial linear polarization (a)

propagating through a vortex retarder, produces a vortex beam with purely radial polarization (c), which can be transformed into a double-lobed, burger-like structure via a polarizer (d). Here, the light field at the two lobes has opposing polarization, which can also be viewed as a phase shift of π , creating a line of zero intensity passing through the center of the beam, whose orientation depends on the orientation of the polarizer. Again, we emphasize here that the zero-intensity line viewed in the 2D profile of the double-lobed beam actually corresponds to a zero-intensity plane extending along the beam propagation direction. Assuming the polarizer to block the \hat{y} component of the electric field, the final beam intensity can be obtained from Eq. (18) as

$$I'_{\text{out}}(\vec{r}) = |E_{\text{out},x}|^2 = \left| \tilde{E}_{\text{out}}(\rho, z) \right|^2 \cos^2 \varphi. \quad (23)$$

In general, the beam curvature α at the center of this beam is now a function of the coordinate y . However, in first order approximation this dependency can be neglected and the intensity profile close to the center can be described by a parabolic function $I \approx \frac{1}{2}\alpha x^2$. As in the case of vortex beams, this curvature scales linearly with the beam power, making the burger-like beams also suitable to be used to shape atomic clouds with the methods described in this paper, allowing for the creation of thin atomic sheets.

It should be noted that a Gaussian beam with a different orientation of its linear polarization than the one shown in Fig. 1a will produce a vortex beam with a different polarization distribution (e.g. purely azimuthal or with both radial and azimuthal components), but can always be converted into a burger-like beam with a polarization filter.

B. Cloud Shaping

Having developed a theoretical understanding of vortex beams, we now describe how they can be used to shape atomic clouds into thin line-like distributions. Following section II A, the intensity profile at the vortex beam center can be approximated with a parabolic function of curvature α , which scales linearly with the beam power P

$$I(\rho) = \frac{1}{2} \alpha \rho^2, \quad \alpha = \alpha_0 P \quad (24)$$

with α_0 being the curvature per beam power and $\rho = \sqrt{x^2 + y^2}$ the radial coordinate for a beam propagating along the z -axis. In general, the curvature α depends on the propagation distance z as the beam expands (cf. Eq. (22)). However, this dependence is negligible on the scale of the atomic cloud size σ_0 , with $\sigma_0 \ll z_0$, hence we assume the curvature to be constant. In the following, the basic principle of cloud shaping is described in an oversimplified picture, which might appear to be too

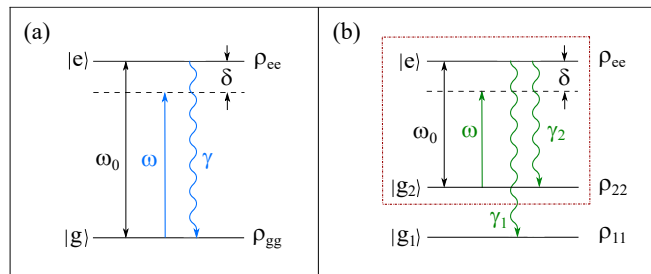


FIG. 2. **Shaping Schemes.** Atomic level schemes for the theoretical description of (a) the *dynamic*- and (b) the *dark-state* shaping methods.

crude at this point, but which offers a simple understanding of the shaping mechanism and yields the same scaling as the full model, presented later on. Let us start by assuming the existence of a critical intensity I_c above which atoms effectively interact with the beam. Then, we can define a critical distance ρ_c from the beam center at which the interaction starts

$$\rho_c = \sqrt{\frac{I_c}{\alpha}} \propto \frac{1}{\sqrt{P}}. \quad (25)$$

The extent $2\rho_c$ of the cloud region in which the atoms do not interact with the vortex beam can thus be arbitrarily reduced (even below the optical diffraction limit) by increasing the beam power. Effectively removing the atoms from the bright beam regions at $\rho > \rho_c$ will then result in a thin line-like atomic distribution.

Various shaping schemes can be employed. Here, we focus on the following two. The first *dynamic scheme* (see Sec. II C) exploits the momentum transfer from resonantly scattered light to accelerate and effectively remove atoms from the bright beam regions of the cloud illuminated by the vortex beam. The second *dark-state scheme* (see Sec. II D) makes use of optical pumping to transfer atoms in bright beam regions to a so-called dark state, which does not interact with the vortex beam.

C. Dynamic Shaping

For a theoretical description of the dynamic shaping scheme, we choose an atom with a closed transition between two states, such that it can be described as a two-level system $|g\rangle$ and $|e\rangle$, with a resonant transition frequency ω_0 (cf. Fig. 2a).

The shaping beam with frequency ω couples the two states and accelerates the atoms along its propagation direction due to the momentum transfer during successive absorption-emission cycles in the scattering process. The force experienced by a single atom is then given by

$$\vec{F}_s(\vec{r}, \dot{\vec{r}}) = \hbar \vec{k} \Gamma(\vec{r}, \dot{\vec{r}}), \quad (26)$$

with $\hbar \vec{k}$ being the momentum carried by a single photon and $\Gamma(\vec{r}, \dot{\vec{r}})$ the photon scattering rate. This can be

calculated as the product of the occupation probability of the excited state ρ_{ee} , obtained from the steady-state solution of the optical Bloch equation accounting for the Doppler effect, and its natural decay rate γ , resulting in

$$\Gamma(\vec{r}, \dot{\vec{r}}) = \rho_{ee}\gamma = \frac{\gamma}{2} \frac{S(\vec{r})}{1 + S(\vec{r}) + \frac{4(\delta + \vec{k} \cdot \dot{\vec{r}})^2}{\gamma^2}}. \quad (27)$$

Here, $S(\vec{r}) = I(\vec{r})/I_{\text{sat}}$ is the saturation parameter, with I_{sat} the saturation intensity, and $\delta = \omega_0 - \omega$ is the frequency detuning. Notice how Γ and \vec{F}_s depend on both the atom position \vec{r} and velocity $\dot{\vec{r}}$, due to the non-homogeneous intensity profile of the shaping beam and the influence of the Doppler shift. Taking into account the gravitational force $\vec{F}_g = m\vec{g}$ with the atomic mass m and gravitational acceleration \vec{g} , the dynamics of the illuminated cloud is then fully described by solving the corresponding equation of motion

$$\frac{\vec{F}_s(\vec{r}, \dot{\vec{r}}) + \vec{F}_g}{m} = \frac{d^2\vec{r}}{dt^2}. \quad (28)$$

The complexity of Eq. (28) arises from the dependence of the scattering force on both the atomic position and velocity, which also translates in an increasing Doppler shift and decreasing scattering rate during the time evolution. Therefore, Eq. (28) has to be solved for all individual atoms making use of numerical methods.

D. Dark-State Shaping

For the dark-state shaping scheme we choose an atom with two hyperfine ground states $|g_1\rangle$ and $|g_2\rangle$ and one excited state $|e\rangle$, which allows for optical pumping between the hyperfine levels. The three-level system is illustrated in Fig. 2b, where we indicated also the time dependent populations $\rho_{ii}(t)$, $i \in \{1, 2\}$ and $\rho_{ee}(t)$. Initially, all atoms are in the upper hyperfine state, i.e. $\rho_{22}(0) = 1$, $\rho_{11}(0) = \rho_{ee}(0) = 0$. The vortex beam with frequency ω couples the state pair $|g_2\rangle - |e\rangle$ with a resonant transition frequency ω_0 , while $|g_1\rangle$ is assumed to be decoupled from the laser and therefore dark. The excited state has a total decay rate $\gamma = \gamma_1 + \gamma_2$, given as sum over the rates γ_1 and γ_2 of the individual decay channels $|e\rangle \rightarrow |g_1\rangle$ and $|e\rangle \rightarrow |g_2\rangle$, respectively.

To describe the time dynamics during the vortex illumination, we use a simple rate picture in combination with the steady-state solution of the optical Bloch equation. The latter allows to specify the time-independent relative population

$$\tilde{\rho} = \frac{\rho_{ee}}{\rho_{22} + \rho_{ee}} = \frac{1}{2} \frac{S(\vec{r})}{1 + S(\vec{r}) + \frac{4\delta^2}{\gamma^2}}, \quad (29)$$

again with $S(\vec{r}) = I(\vec{r})/I_{\text{sat}}$ and $\delta = \omega_0 - \omega$. Note that, in contrast to Eq. (27), we neglected here the Doppler shift,

as typically only a few photons need to be scattered before the atom is pumped to the $|g_1\rangle$ dark state. With typical alkali recoil velocities $\hbar k/m$ on the order of 10 mm/s and resulting Doppler shifts $\hbar k^2/m$ of about $2\pi \times 10$ kHz, this is justified, as for few scattering events the total Doppler shift stays well below the natural linewidth γ , which is typically 2-3 orders of magnitude larger.

Using Eq. (29), the change in the overall population of the coupled $|g_2\rangle - |e\rangle$ system can now be described with a differential equation in terms of the decay rate γ_1

$$\frac{d}{dt}(\rho_{22} + \rho_{ee})(t) = -\gamma_1\rho_{ee}(t) = -\gamma_1\tilde{\rho}(\rho_{22} + \rho_{ee})(t).$$

Considering the initial condition $(\rho_{22} + \rho_{ee})(0) = 1$, the solution exhibits a simple exponential decay

$$(\rho_{22} + \rho_{ee})(t) = e^{-\gamma_{\text{eff}}t}, \quad (30)$$

where we have defined the effective decay rate of the coupled $|g_2\rangle - |e\rangle$ system to the dark ground state $|g_1\rangle$ as $\gamma_{\text{eff}} = \gamma_1\tilde{\rho}$. The time evolution for the populations of the individual states then become

$$\begin{aligned} \rho_{11}(t) &= 1 - e^{-\gamma_{\text{eff}}t} \\ \rho_{22}(t) &= (1 - \tilde{\rho})e^{-\gamma_{\text{eff}}t} \\ \rho_{ee}(t) &= \tilde{\rho}e^{-\gamma_{\text{eff}}t}. \end{aligned} \quad (31)$$

Notice that Eqs. (31) only represent an approximation to the real populations evolution, which is obtained by solving the set of three coupled rate equations describing the complete three-level system. However, the timescale at which the $|g_2\rangle - |e\rangle$ system reaches the steady-state is much faster than the populations decay, therefore our simplified description well approximates the real time evolution.

It is now convenient to write γ_{eff} as a function of the modified saturation parameter $\tilde{S}(\vec{r}) = I(\vec{r})/\tilde{I}_{\text{sat}}$, where the non-resonant saturation intensity is $\tilde{I}_{\text{sat}} = I_{\text{sat}}(1 + 4\delta^2/\gamma^2)$. Using Eq. (29), we obtain

$$\gamma_{\text{eff}}(\vec{r}) = \gamma_1\tilde{\rho} = \frac{\gamma_1}{2} \frac{\tilde{S}(\vec{r})}{1 + \tilde{S}(\vec{r})}. \quad (32)$$

In the case of a shaping vortex beam, the intensity profile at the beam center is approximately parabolic (cf. Eq. (24)), such that the saturation parameter also has a parabolic shape. Assuming the beam to propagate along the z-axis

$$\tilde{S}(x, y) = \frac{I(x, y)}{\tilde{I}_{\text{sat}}} = \frac{1}{2} \tilde{\beta}_0 P(x^2 + y^2) \quad (33a)$$

$$\tilde{\beta}_0 = \frac{\alpha_0}{\tilde{I}_{\text{sat}}}. \quad (33b)$$

Combining Eqs. (32) and (33a), it is evident how the atoms in the cloud are pumped to the $|g_1\rangle$ dark state in

a spatially-dependent way, with the ones at the center of the vortex beam remaining unperturbed.

To find an analytical expression for the size of the shaped atomic cloud after some vortex beam illumination time τ_{ill} , we assume a Gaussian density profile $\rho_0(\vec{r})$ for the initial cloud

$$\rho_0(\vec{r}) = \rho_0 \exp\left(-\frac{x^2}{2\sigma_{0,x}^2} - \frac{y^2}{2\sigma_{0,y}^2} - \frac{z^2}{2\sigma_{0,z}^2}\right) \quad (34)$$

with characteristic widths $\sigma_{0,i}$, $i \in \{x, y, z\}$. Also, we assume the cloud expansion during the vortex beam illumination to be negligible, which is valid in the limit of $\tau_{\text{ill}} \ll \sigma_{0,i} \sqrt{m/k_B T}$ for a Boltzmann-Gaussian velocity distribution [31]. For a vortex beam centered at the cloud position, the atomic distribution after τ_{ill} can then be calculated as

$$\begin{aligned} \rho(\vec{r}, \tau_{\text{ill}}) &= \rho_0(\vec{r}) e^{-\gamma_{\text{eff}} \tau_{\text{ill}}} \quad (35) \\ &\approx \rho_0(\vec{r}) \exp\left(-\frac{\gamma_1}{2} \tilde{S}(x, y) \tau_{\text{ill}}\right), \quad (36) \end{aligned}$$

where we have assumed $\tilde{S} \ll 1$ in Eq. (32) close to the center of the vortex beam. Inserting $\tilde{S}(x, y)$ from Eq. (33a) and defining

$$\sigma_s(P, \tau_{\text{ill}}) = \left(\frac{\gamma_1}{2} \tilde{\beta}_0 \tau_{\text{ill}} P\right)^{-\frac{1}{2}}, \quad (37)$$

the exponential function in Eq. (36) can be expressed as a Gaussian of width σ_s in the coordinates x and y , such that the final atomic distribution becomes

$$\rho(\vec{r}, \tau_{\text{ill}}) \approx \rho_0 \exp\left(-\frac{x^2}{2\sigma_s^2} - \frac{y^2}{2\sigma_s^2} - \frac{z^2}{2\sigma_{0,z}^2}\right), \quad (38)$$

with

$$\frac{1}{\sigma_i^2} = \frac{1}{\sigma_s^2} + \frac{1}{\sigma_{0,i}^2}, \quad i \in \{x, y\}. \quad (39)$$

It is now evident that the vortex beam shapes the density distribution of the atomic cloud in the x-y plane, while leaving it unaffected along z. Inserting Eq. (37) in Eq. (39) and substituting the definition of $\tilde{\beta}_0$ from Eq. (33b), one finds the effective width σ_i along the axis $i \in \{x, y\}$ to be

$$\sigma_i = \sigma_{0,i} \left(1 + \sigma_{0,i}^2 \frac{\gamma_1}{2} \frac{\alpha_0}{I_{\text{sat}} \left(1 + \frac{4\delta^2}{\gamma^2}\right)} E_{\text{ill}}\right)^{-\frac{1}{2}}, \quad (40)$$

where we defined the total energy of the vortex pulse as $E_{\text{ill}} = P \tau_{\text{ill}}$. In the limit of large energies, the shaped cloud width does not depend on the initial size anymore, but only on the beam parameters

$$\sigma_i \approx \sigma_s = \left(\frac{\gamma_1}{2} \frac{\alpha_0}{I_{\text{sat}} \left(1 + \frac{4\delta^2}{\gamma^2}\right)} E_{\text{ill}}\right)^{-\frac{1}{2}} \propto E_{\text{ill}}^{-\frac{1}{2}}. \quad (41)$$

According to this theoretical model, the size of the shaped cloud follows a power-law dependence on the energy of the vortex pulse and can therefore be reduced arbitrarily for increasing E_{ill} .

III. EXPERIMENTAL SETUP

Our experimental setup used for the generation and shaping of atomic clouds is illustrated in Fig. 3a. It is built upon a standard six-beam magneto-optical trap (MOT) for ^{87}Rb atoms, operated inside a vacuum chamber at a pressure of $2 \cdot 10^{-10}$ mbar. All lasers required for MOT operation, cloud shaping and cloud imaging are guided via optical viewports into the chamber and operated near the rubidium D₂ line, with the specific transition frequencies given in Fig. 3b. The cooling beam with a waist of 8 mm and a total power of 150 mW is 15 MHz red detuned with respect to the $|5S_{1/2}, F=2\rangle \rightarrow |5P_{3/2}, F'=3\rangle$ cooling transition. Atoms that get off-resonantly excited to the $|5S_{1/2}, F'=2\rangle$ state and decay to the $|5S_{1/2}, F=1\rangle$ ground state are pumped back to the cooling cycle via a repumping beam of 8 mm waist and 10 mW power, which is tuned resonant to the $|5S_{1/2}, F=1\rangle \rightarrow |5P_{3/2}, F'=2\rangle$ transition.

For MOT operation, the cooling and repumping light are superimposed and split up in three counter-propagating beam pairs, mutually overlapping at the center of the vacuum chamber. Here, a pair of Anti-Helmholtz coils creates a magnetic quadrupole field with vanishing field at the center and field gradients of 7.5 and 15 G/cm in x-y and z-direction, respectively. Altogether, this creates an optical molasses, which allows for trapping and cooling atoms, loaded directly from a Rb dispenser source nearby. The generated cloud represents the starting point for the shaping experiments, after which the cloud is imaged via standard absorption imaging. For this, the cloud is illuminated with an imaging beam of 5 mm waist and 80 μW power, tuned resonant to the $|5S_{1/2}, F=2\rangle \rightarrow |5P_{3/2}, F'=3\rangle$ transition, and the resulting beam transmission $G(\tilde{x}, \tilde{y})$ is measured on a CCD camera. Together with two reference images (a background image $B(\tilde{x}, \tilde{y})$ without atoms and a dark image $D(\tilde{x}, \tilde{y})$ without light), this allows to determine the integrated atomic density $n_{2D}(\tilde{x}, \tilde{y})$ in the plane perpendicular to the imaging axis \tilde{z} [31]

$$n_{2D}(\tilde{x}, \tilde{y}) = \int n(\vec{r}) d\tilde{z} = -\frac{1}{\sigma_{\text{Rb}}} \ln \frac{G(\tilde{x}, \tilde{y}) - D(\tilde{x}, \tilde{y})}{B(\tilde{x}, \tilde{y}) - D(\tilde{x}, \tilde{y})}, \quad (42)$$

with the photon scattering cross section σ_{Rb} . This is a direct consequence of Lambert-Beers law, upon which the beam transmission decays exponentially with the optical depth $\sigma_{\text{Rb}} n_{2D}(\tilde{x}, \tilde{y})$.

The shaping beam propagates along the z-axis, forming an angle of about 35° with the imaging beam (cf. Fig. 3a), and is stabilized to different transitions depending on which shaping method is used (cf. Fig. 3b). For the *dynamic scheme*, we use the

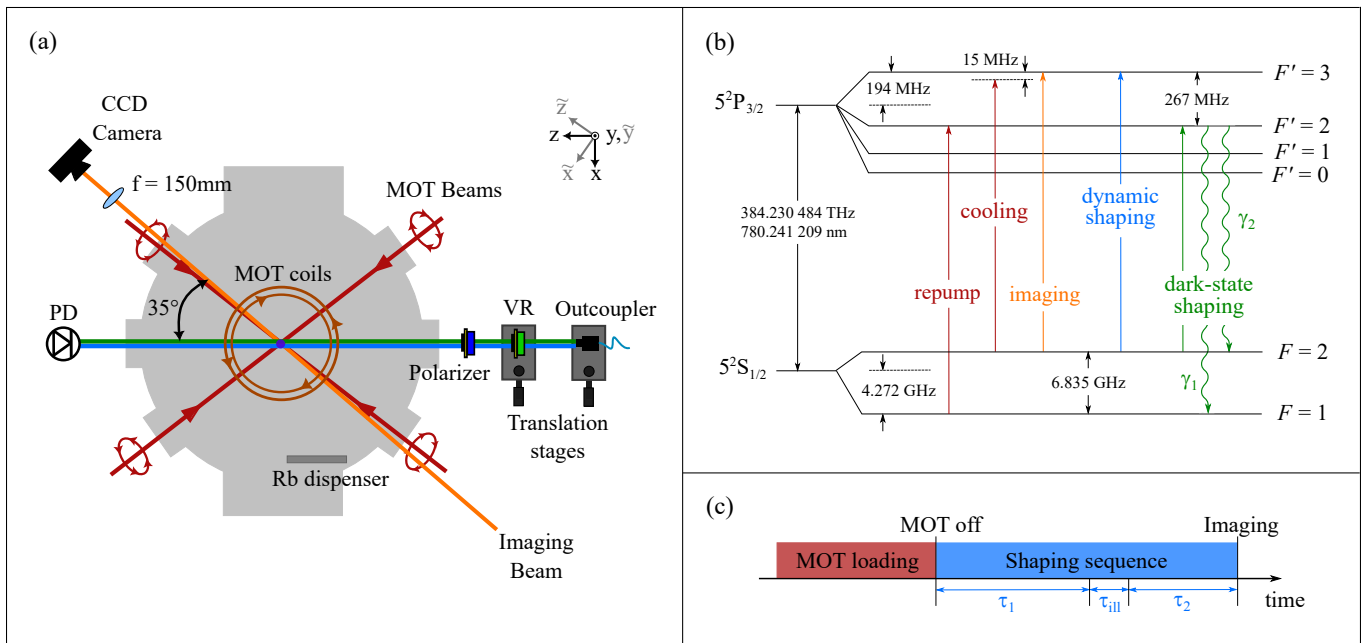


FIG. 3. **Experimental Realization.** (a) Experimental setup for the generation and shaping of an atomic cloud. A six-beam magneto-optical trap (MOT) is operated inside a vacuum chamber, whose lateral view-ports offer optical access to the lasers required for MOT operation, cloud imaging and shaping. The Gaussian intensity profile of the shaping beam coming out of the fiber is transformed into a vortex via the vortex retarder (VR) or into a double-lobed, burger-like structure via the additional polarizer. The beam power during the shaping pulse is monitored via a photodiode (PD). Gravity is pointing in negative y -direction. (b) Level scheme of the ^{87}Rb D2-line and transition frequencies for the lasers used in the experiment. The shaping light is tuned to different transitions, depending on the shaping method used. (c) Measurement procedure for the shaping of an atomic cloud generated from a MOT. After the MOT loading, the cloud is left free to thermally expand during τ_1 , after which it is illuminated by the shaping light during τ_{ill} and then freely expands again during τ_2 , before being imaged.

closed $|5S_{1/2}, F=2\rangle \rightarrow |5P_{3/2}, F'=3\rangle$ transition. For the *dark-state scheme*, atoms are excited from the $|5S_{1/2}, F=2\rangle$ to the $|5P_{3/2}, F'=2\rangle$ state and therefore effectively pumped to the $|5S_{1/2}, F=1\rangle$ ground state, which is dark to both shaping and imaging light. For the generation of the vortex beam, we employ a zero-order vortex half-wave retarder with $m=1$, which transforms the collimated Gaussian beam, with waist $w_0=1$ mm, coming out of a polarization maintaining (PM) fiber into the desired vortex intensity profile. In the case of the dynamic shaping scheme, for better visualization, an additional polarization filter is placed after the vortex retarder in order to create a double-lobed, burger-like beam, which allows for the creation of a thin atomic sheet. Both the fiber outcoupler and the vortex retarder are placed on a x - y micro translation stage to ensure that the shaping beam is centered at the atom cloud and the vortex retarder, respectively.

The measurement procedure, highlighted in Fig. 3c, is as follows. First, the MOT is loaded for appropriate times up to 14.5 s. The switching off of the cooling and repump beams defines the start of the shaping sequence, during which the cloud expands and falls under the constrain of the shaping beam. The atomic cloud is first left free to expand for a time τ_1 , such that at the end it attains an approximately 3D Gaussian distribution. Next,

the cloud is illuminated by the shaping beam, which is pulsed for a variable time τ_{ill} . Finally, the cloud again freely evolves for a waiting time τ_2 (only needed for the dynamic shaping scheme), after which it is imaged. The pulse duration τ_{ill} and the relative beam power are monitored by means of a fast photodiode, which is placed at the end of the shaping beam path outside the MOT chamber.

IV. RESULTS

A. Dynamic shaping

For the dynamic shaping, we present experimental results and compare them to numerical simulations introduced in Sec. II C. In particular, we investigate the dependence of the atoms dynamics on the choice of different experimental parameters, such as the beam power and the timings during the shaping sequence (cf. Fig. 3c). For better visualization of the cloud dynamics, we choose to use a double-lobed, burger-like beam, as shown in Fig. 1d, and rotate its intensity zero plane via the polarizer to be parallel to the x - z plane (cf. Fig. 3a). This means that the cloud gets shaped along the vertical y -axis, with the atoms being accelerated along the propagation direction

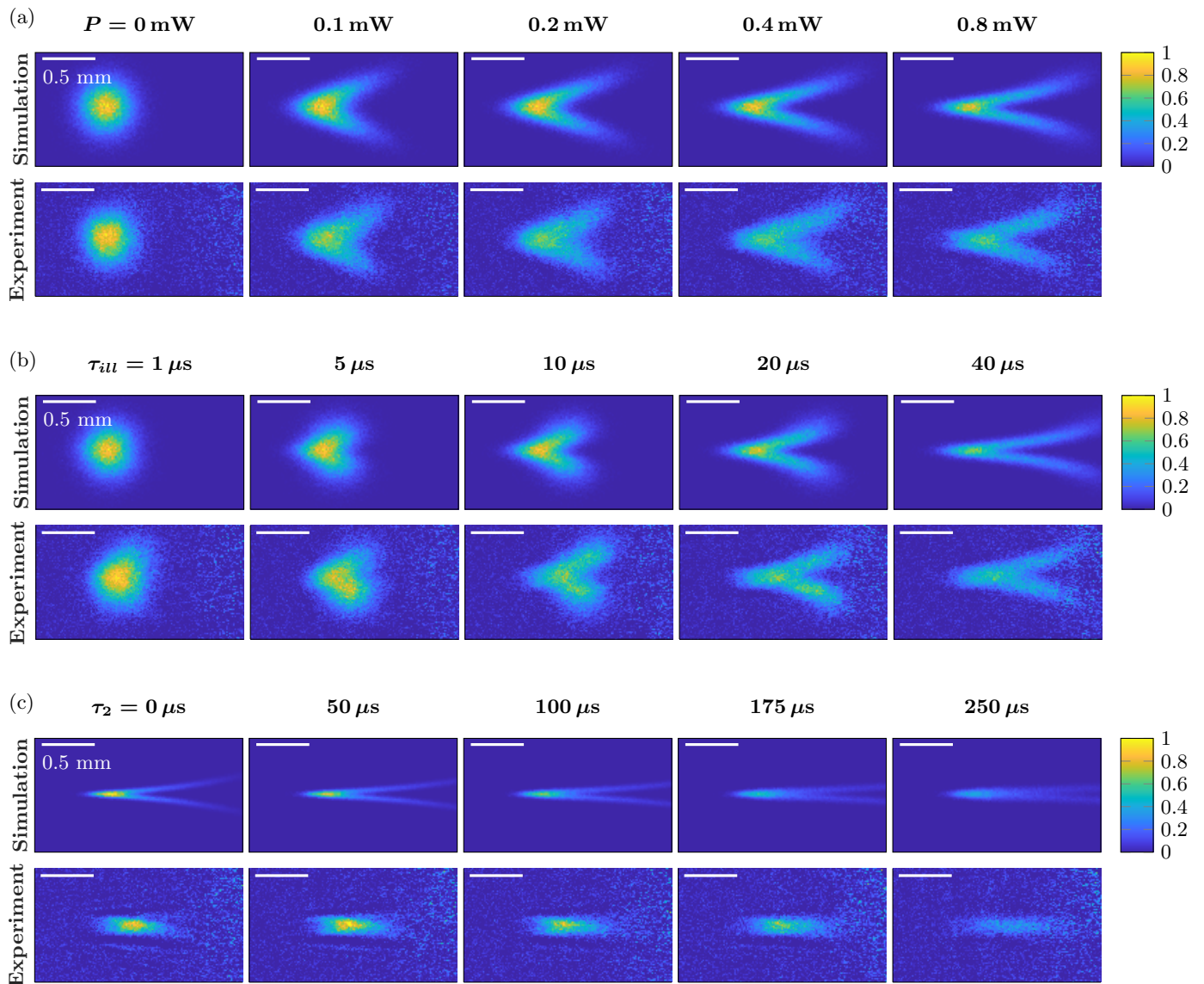


FIG. 4. **Dynamic shaping with burger-like beam.** Absorption images as simulated (upper rows) and measured (lower rows) for a series of increasing (a) shaping beam power P , with $\tau_1 = 1.2$ ms, $\tau_{\text{ill}} = 35$ μs , $\tau_2 = 565$ μs , (b) illumination time τ_{ill} , with $\tau_1 = 1.2$ ms, $\tau_2 = 565$ μs , $P = 1.45$ mW, and (c) free expansion time after the shaping τ_2 , with $\tau_1 = 200$ μs , $\tau_{\text{ill}} = 300$ μs , $P = 1.45$ mW. All images are shown in the \tilde{x} - \tilde{y} plane, with the shaping beam irradiated from the left. In the simulated images, we set $\beta_0 = 2.2 \cdot 10^4$ $\text{mW}^{-1}\text{cm}^{-2}$ and the visibility of the atoms is adjusted depending on their final velocity to account for the Doppler shift with respect to the imaging beam. All images are normalized to the maximum atom density within the first image of each individual row, both for simulations and experiments.

of the shaping beam (z). For every choice of parameters, the cloud is imaged in the \tilde{x} - \tilde{z} plane via absorption imaging. For the measurements presented in this section, the starting point of the shaping sequence is a cloud of $\approx 5 \cdot 10^5$ atoms at a temperature $T \approx 45$ μK , with an initial size in the vertical direction $\sigma_{0,y} \approx 100$ μm .

In order to reproduce these conditions in the numerical simulations, we consider a cloud of N atoms, whose initial positions along the three axes are sampled from Gaussian distributions of widths $\sigma_{0,i} = \sigma_{0,y}$ (assuming the cloud to be isotropic), while the initial velocities are sampled from

a three-dimensional Boltzmann distribution with temperature T , i.e. a Gaussian with width $\sigma_v = \sqrt{k_B T/m}$. The shaping beam is approximated with a parabolic intensity profile $I(x, y) = \frac{1}{2} \alpha_0 P y^2$, where the central curvature per power is $\alpha_0 = 1.55 \cdot 10^5$ cm^{-4} . This value is obtained from a fit to a vertical line-scan passing through the center of the beam, imaged via a CMOS camera as it appears at the cloud position, and is assumed to be constant on the spatial scale of the cloud. In the simulations, the relevant quantity is the curvature per power of the saturation parameter $S(x, y) = I(x, y)/I_{\text{sat}}$, defined as $\beta_0 = \alpha_0/I_{\text{sat}}$,

which can be adapted to get a good qualitative match with the experimental pictures and therefore obtain an estimation of the saturation intensity for the driven transition. The equation of motion in (28) is solved for the entire duration of the shaping sequence, using the ode45 solver from Matlab. In our specific case, the gravitational force is directed along the vertical y-axis, while the scattering force acts along the z-axis and is non-zero only during the illumination time τ_{ill} . To allow for a direct comparison of the simulated cloud with the experimental measurement, the x-y view of the resulting atomic distribution is rotated by 35° into the imaging plane \tilde{x} - \tilde{y} (cf. Fig. 3a). Additionally, the visibility of each atom is adjusted depending on its final velocity, in order to account for the Doppler shift δ_D with respect to the imaging beam. In fact, from our simulations, we find that at the end of the shaping pulse the atoms can reach velocities along the z-axis up to 15 m/s, which translates to a Doppler shift of about $\delta_D = 2\pi \times 16$ MHz when accounting for the 35° angle formed by the imaging beam. This is about a factor of three larger than the natural linewidth of the imaging beam transition, which according to the Lorentzian absorption profile, reduces the atoms visibility (photon scattering rate) to about 3% of its original value.

Figure 5 shows the results of measurement series and corresponding simulations for the cloud shaping with a resonant beam for increasing (a) beam power P , (b) illumination time τ_{ill} and (c) free expansion time after shaping τ_2 . In the simulations, we fix $\beta_0 = 2.2 \cdot 10^4 \text{ mW}^{-1} \text{ cm}^{-2}$, which results in a saturation intensity of $I_{\text{sat}} = 7.2 \text{ mW cm}^{-2}$. This value is about double the expected saturation intensity of 3.3 mW cm^{-2} , which is calculated for the driven transition considering the steady-state population distribution between the magnetic sub-levels (cf. Appendix B). This discrepancy could be attributed to a non-perfect alignment between the shaping beam and the cloud in x-direction: due to the finite size of the beam, a horizontal offset of about $350 \mu\text{m}$ is sufficient to reduce the curvature per power α_0 by a factor 2, hence doubling the estimated saturation intensity for the chosen β_0 .

For the first measurement series, the timings in the shaping sequence are set to $\tau_1 = 1.2 \text{ ms}$, $\tau_{\text{ill}} = 35 \mu\text{s}$, $\tau_2 = 565 \mu\text{s}$ and the cloud is imaged at different beam powers P , ranging from 0 to 0.8 mW . The experimental measurements and numerical simulations show very good agreement (cf. Fig. 4a), highlighting how atoms get pushed away from the upper and lower regions of the cloud in the shape of two wings. A first aspect to be noticed is that the size of the remaining atomic layer decreases with increasing power, as expected from increasing the curvature at the center of the shaping beam. Furthermore, some considerations can be made regarding the shape of the lateral wings. In particular, the atomic displacement along the propagation direction of the shaping beam (z) is linearly proportional to the scattering force experienced during the shaping pulse, for which

two extreme conditions can be considered. In the limit of $I \ll I_{\text{sat}}$, the scattering rate, and hence the scattering force, scales linearly with the intensity (cf. Eq. (27)), which for a burger-like beam increases quadratically with the distance of the atoms from the beam center along the vertical y-axis. Therefore, the wings formed by the accelerated atoms should follow a square-root profile (simulations show this effect being mainly visible for powers lower than 0.1 mW , which can just be guessed in Fig. 4a). On the contrary, for $I \gg I_{\text{sat}}$, the force is constant independently of the atom position, ideally resulting in a constant displacement for all atoms away from the beam center. The plots in Fig. 4a show that the wings start bending upwards for increasing beam powers, which can be considered as a sign of saturation effects becoming relevant. However, keep in mind that due to the power broadening, full saturation of the trajectories will only be reached for much larger powers.

A good agreement between measurements and simulations is also found for the second measurement series (cf. Fig. 5b), for which we still use $\tau_1 = 1.2 \text{ ms}$ and $\tau_2 = 565 \mu\text{s}$, but fix the beam power to $P = 1.45 \text{ mW}$ and vary the illumination time τ_{ill} in the range $1 - 40 \mu\text{s}$. Here, the scattering force acts for an increasing time, resulting in an increasing velocity at the end of the shaping pulse and therefore in a larger horizontal displacement of the outer cloud wings from the original position. The similarity between the results in (a) and (b) attests that there is a correlation between the role of the beam power and the illumination time in the shaping mechanism, suggesting that a more relevant quantity is the energy transferred to the atoms during the shaping pulse $E_{\text{ill}} = P \tau_{\text{ill}}$, at least in the limit of short illumination times.

For the third measurement set we use again $P = 1.45 \text{ mW}$, while setting $\tau_1 = 200 \mu\text{s}$, $\tau_{\text{ill}} = 300 \mu\text{s}$ and vary τ_2 in the range $0 - 250 \mu\text{s}$. Here, the long illumination time leads to an almost complete removal of the atoms from the outer regions of the cloud, while leaving the central ones in a thin distribution (cf. Fig. 5c). From a comparison between measurements and calculations, it can be noticed how the measured clouds are generally thicker than the simulated ones, which we attribute to the limited resolution of our imaging system. This hypothesis is supported by the appearance of interference patterns besides the shaped cloud. Also, the simulations show the moving away of the outer atoms, which are completely absent in the experimental pictures. However, the trace is greatly faded even in the simulations due to the Doppler shift caused by the large velocity of the accelerated atoms, which explains the difficulty in imaging them experimentally. Finally, both measurements and simulations show that for increasing τ_2 the cloud also slightly expands along the vertical direction and that the atomic density decreases. This represents one of the main disadvantages of this shaping technique with respect to the *dark-state scheme* presented in the following section. In the *dynamic scheme*, a finite τ_2 is essential for the atoms to fly away from the cloud and thus for the shaping to

occur. However, this partially limits the thinning of the remaining atomic distribution due to thermal expansion of the cloud. For completeness, we mention that a shaping series with fixed power, τ_{ill} and τ_2 and varying τ_1 was also measured. In this case, the final shape of the cloud doesn't change, but the atomic density decreases for increasing τ_1 due to the initial expansion of the cloud before shaping.

B. Dark-state shaping

We now present experimental results and compare them to the theoretical model for the dark-state shaping method, described in section II D, for the case of a vortex beam. In particular, we aim to verify the dependence of the shaped cloud width on the energy of the vortex pulse and its frequency detuning, as described in Eq. (40). For the measurements presented in this section, the starting point of the shaping sequence is represented by a cloud of $\approx 1.5 \cdot 10^6$ atoms at a temperature of $T \approx 15 \mu\text{K}$, with an initial size $\sigma_{0,i} \approx 200 \mu\text{m}$, $i \in \{x, y, z\}$. For a simple quantitative analysis of the cloud images, we focus on the width along the vertical \tilde{y} -axis (corresponding to y), since the imaged horizontal atomic distribution (along \tilde{x}) results from a combination of the x - and z -axis due to the angle between the shaping and the imaging beam (cf. Fig. 3a). To extract the cloud width, 20 absorption images are taken and averaged for every choice of parameters used for the shaping. The resulting picture is integrated along the horizontal \tilde{x} -axis and the integrated signal is fit to a Gaussian function, from which we deduce the vertical width σ_y .

To investigate the energy dependence, the shaping beam is tuned to resonance with the $|5S_{1/2}, F=2\rangle \rightarrow |5P_{3/2}, F'=2\rangle$ transition and we set $\tau_1 = 4.5 \text{ ms}$ and $\tau_2 = 0$. We perform measurement sets at different illumination times τ_{ill} , in the range $10 - 50 \mu\text{s}$, for which we vary the beam power P , ranging from 0 up to about $140 \mu\text{W}$. Figure 5 displays some examples of averaged absorption images from the power series with $\tau_{\text{ill}} = 10 \mu\text{s}$, showing the reduction of the cloud size in the vertical direction with increasing beam power. The different measurement series can be combined in a single data set in which the varying parameter becomes the illumination energy $E_{\text{ill}} = P \tau_{\text{ill}}$, with values up to a maximum of about 2.4 nJ (for $\tau_{\text{ill}} = 50 \mu\text{s}$ and $P = 49 \mu\text{W}$). The extracted widths σ_y as a function of E_{ill} are displayed in Fig. 6, together with the fit to the function in Eq. (40). Here, $\delta = 0$, $\gamma = 2\pi \times 6 \text{ MHz}$ corresponds to the overall decay rate of the excited $|5P_{3/2}, F'=2\rangle$ state, with $\gamma_1 = \gamma_2 = \gamma/2$, and the initial cloud size is fixed to the mean value of the extracted widths from the $P = 0$ measurements, resulting in $\sigma_{0,y} = 209 \mu\text{m}$. Then, the only fit parameter is the curvature per power of the saturation parameter at the beam center $\beta_0 = \alpha_0/I_{\text{sat}} = 7.1 \cdot 10^3 \text{ mW}^{-1}\text{cm}^{-2}$. From characterization measurements of the vortex beam (cf. Appendix A), the vortex intensity cur-

vature per power at the cloud position is estimated to be $\alpha_0 = 1.2 \cdot 10^5 \text{ cm}^{-4}$, yielding $I_{\text{sat}} = 16.3 \text{ mW cm}^{-2}$. This is well within the interval of possible values for the saturation intensity for the $|5S_{1/2}, F=2\rangle \rightarrow |5P_{3/2}, F'=2\rangle$ transition, which can range between $10 - 20 \text{ mW cm}^{-2}$ depending on the initial population distribution among the magnetic sub-levels (cf. Appendix B). The good agreement between the experimental data and the fitted theoretical curve supports our simple theoretical model for the *dark-state scheme*. Because of the radial symmetry of the vortex beam, the same behavior is expected for σ_x , while the extension of the cloud along the propagation direction z remains unaffected. Therefore, the initial atomic distribution is shaped as a cigar-like cloud, whose radial size can be decreased by increasing the shaping beam power or the illumination time.

Our model can be further verified by investigating the dependence of the shaped cloud width on the frequency detuning of the vortex beam. In this case, we again set $\tau_1 = 4.5 \text{ ms}$, $\tau_2 = 0$ and illuminate the cloud for $\tau_{\text{ill}} = 10 \mu\text{s}$ with a beam power of approximately $130 \mu\text{W}$, corresponding to $E_{\text{ill}} = 1.3 \text{ nJ}$. The detuning δ is varied in the range between $\pm 2\pi \times 20 \text{ MHz}$, with $\delta > 0$ and $\delta < 0$ indicating red- and blue-detunings, respectively. The results are shown in Fig. 7. Here, the fit function is

$$\sigma_y = \frac{\sigma_{0,y}}{\sqrt{1 + \sigma_{0,y}^2 \frac{\gamma_1}{2} \frac{\beta_0}{1 + \left(\frac{2c(\delta - \delta_0)}{\gamma}\right)^2} E_{\text{ill}}}}, \quad (43)$$

where the fit parameters c and δ_0 are introduced to take into account possible deviations of the frequency detuning with respect to the set value. The unperturbed cloud size $\sigma_{0,y}$ is fixed as in the previous case and $\gamma_1 = 2\pi \times 3 \text{ MHz}$ corresponds to the rate of the single decay channel from $|5P_{3/2}, F'=2\rangle$ to the dark $|5S_{1/2}, F=1\rangle$ state. We obtain $c = 1.36$, $\delta_0 = -2\pi \times 0.13 \text{ MHz}$ and $\beta_0 = 8.6 \cdot 10^3 \text{ mW}^{-1}\text{cm}^{-2}$, corresponding to a saturation intensity of $13.5 \frac{\text{mW}}{\text{cm}^2}$. Again, this value lies within the expected interval and the good agreement between the experimental data and the fitted curve further validates our theoretical model. Notice that the data show no difference between positive and negative detunings, meaning that only the absolute value is relevant, as predicted by the theory. Increasing the detuning has the only effect of reducing the scattering rate of the shaping beam photons from the atoms in the cloud and therefore of increasing the final cloud size. For the creation of narrow line-shaped atomic clouds, a resonant shaping beam is thus a more convenient choice, since it allows to generate thinner distributions at a much lower beam power.

V. DISCUSSION AND CONCLUSION

In this work, we have presented a method for shaping an unconfined cold atomic cloud by a vortex laser beam

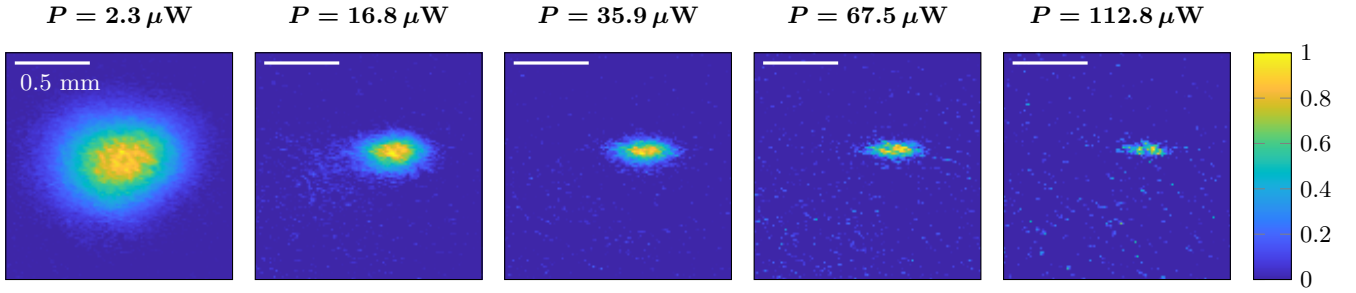


FIG. 5. **Dark-state shaping with vortex beam.** Absorption images for a measurement series of increasing vortex beam power P , with fixed timings for the shaping sequence $\tau_1 = 4.5$ ms, $\tau_{\text{ill}} = 10$ μ s, $\tau_2 = 0$. All images result from the average of 20 pictures and are shown in the \bar{x} - \bar{y} plane, normalized to the maximum atom density in each image. Between the first and the last picture, the atomic column density is reduced by more than three orders of magnitude.

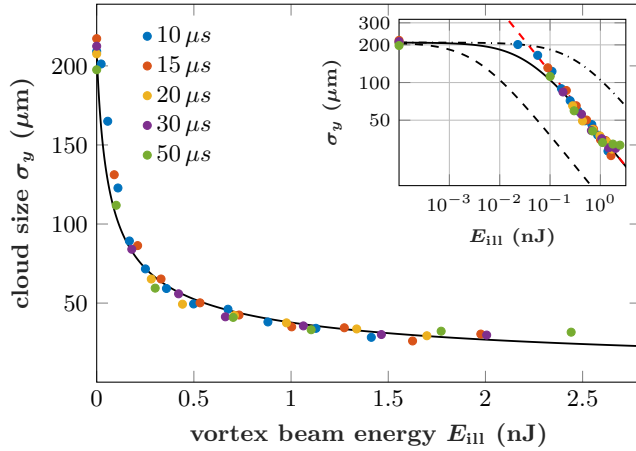


FIG. 6. **Energy dependence.** Cloud size along the vertical direction σ_y as a function of the energy of the vortex pulse E_{ill} . The colored dots represent experimental data, with the different colors corresponding to different illumination times τ_{ill} , while the solid black line represents the fit to the common logarithm of the function in Eq. (40). The inset shows the same plot with a log-log scale, with the dashed red line highlighting the $E_{\text{ill}}^{-1/2}$ dependence at high energy. The black dashed- and dashed-dotted lines show the theoretical behavior for a curvature per beam power of $10\alpha_0$ and $\alpha_0/10$ respectively, with $\alpha_0 = 1.2 \cdot 10^5$ cm^{-4} being the measured curvature per beam power at the center of the vortex beam (cf. Appendix A).

having a polarization singularity at the center. We provided an analytic description for the beam electric field produced by a vortex retarder, demonstrating that the intensity close to the center can be approximated with a parabola whose curvature scales linearly with the beam power. Experimentally, we demonstrated two different shaping schemes for a free expanding atomic cloud generated from a MOT of ^{87}Rb atoms: the *dynamic scheme*, in which atoms in bright beam regions are accelerated and effectively removed from the cloud, and the *dark-state scheme*, in which atoms are pumped to a state not interacting with the vortex light. In the first case, we showed

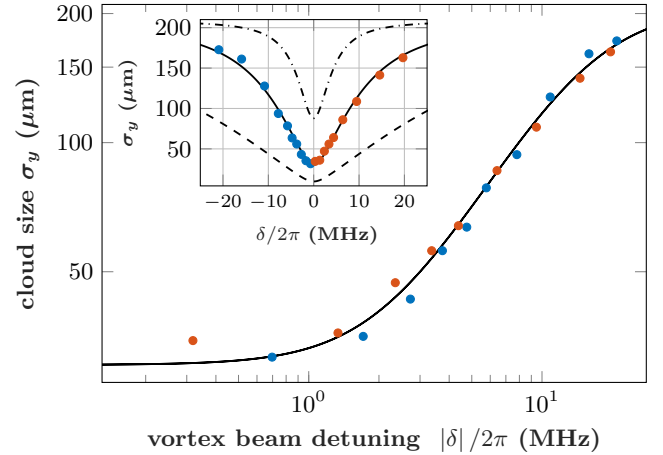


FIG. 7. **Detuning Dependence.** Cloud size along the vertical direction σ_y as a function of the absolute value of the detuning of the vortex pulse $|\delta|$, shown with a log-log scale. The colored dots represent experimental data at $E_{\text{ill}} = 1.3$ nJ, with the colors red and blue corresponding to red and blue detuning respectively, while the solid black line represents the fit to the function in Eq. (43). The unfolded plot is shown in the inset with a lin-lin scale. The black dashed- and dashed-dotted lines show the theoretical behavior for illumination energies $10 E_{\text{ill}}$ and $E_{\text{ill}}/10$, respectively.

a qualitative comparison of absorption imaging pictures of the shaped cloud with numerical simulations for different parameters, finding good agreement. For the second method, we developed a simple theoretical model to quantitatively describe the thickness of the shaped cloud as a function of some experimental parameters, such as the energy in the shaping pulse and the frequency detuning, which well fits our experimental data.

The *dark-state scheme* can be used to generate thin line- or sheet-like atomic clouds in the case of state-selective measurements and offers significant advantages with respect to the *dynamic scheme*. First, the optical pumping to the ground dark state occurs on a much faster timescale and with a much lower beam power compared to the dynamic removal of the atoms, such that

the illumination time τ_{ill} and P can in general be reduced. Also, this method requires no additional free evolution time τ_2 after the illumination pulse, preventing the atomic cloud from expanding again and therefore increasing its final size. Finally, differently from the *dynamic scheme*, in this case the atoms are not physically removed from the cloud, making it possible to restore the original atomic distribution by pumping them back to the non-dark state, for example by using the MOT repump beam. In view of the envisioned Rydberg interaction experiments involving typical cycles of cloud shaping, Rydberg excitation and -interaction, and detection, high cycle rates are preferable. With a few milliseconds between individual cycles to reload the MOT from the dark state and to compensate for eventual losses, the *dark-state scheme* would then allow for repetition rates of few hundreds cycles per second.

Currently, the limited resolution of our imaging system prevents us from detecting clouds with a thickness below $\sigma_y \approx 30 \mu\text{m}$. However, the fit of our theoretical model to the experimental data predicts that a cloud size on the order of $\sigma_y \approx 2.7 \mu\text{m}$ can be created with a beam energy of $E_{\text{ill}} \approx 200 \text{ nJ}$. Considering an illumination time $\tau_{\text{ill}} = 10 \mu\text{s}$, which is the shortest used in our experiment, this translates in a required power of only 20 mW, which is easily achievable in diode laser setups. In a diffraction-limited system involving a dipole sheet, the creation of a clouds with similar size would typically require a focusing lens with a numerical aperture of approximately 0.3, placed close to the atoms. Here, however, we use a beam of 1 mm waist, which can be prepared meters away from the atom cloud.

In summary, the fast timescale, the requirement of low power and the very simple setup makes our *dark-state shaping scheme* particularly appealing for micron-sized shaping of unconfined atom clouds, providing an easily accessible and practical experimental platform for studies with thin atomic ensembles.

ACKNOWLEDGEMENTS

The authors would like to thank Philip Osterholz for helpful discussions on the experiment. This work was supported by the Deutsche Forschungsgemeinschaft through FOR 5413.

Appendix A: Vortex beam

Here, we present a characterization measurement of the vortex beam used for the dark-state shaping presented in Sec. IV B, aiming to estimate the parameter α_0 from Eq. (24). Therefore, the shaping beam is deflected in front of the chamber and imaged via a CMOS camera, placed at the same distance to the vortex retarder as the MOT. Thus, the beam profile resembles the one at the MOT position. To correct for the black level of the

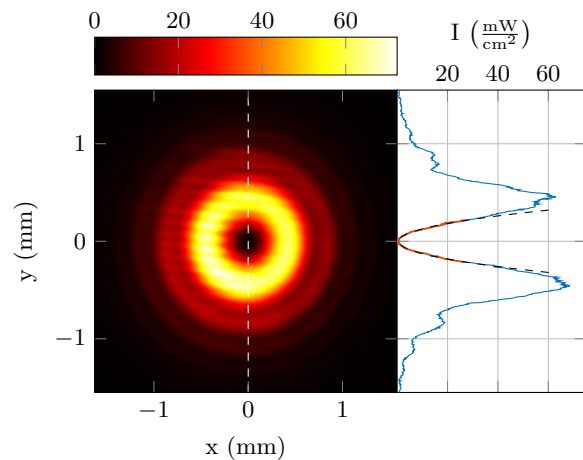


FIG. 8. **Vortex beam.** Intensity profile of the vortex beam as imaged with a CMOS camera at the MOT position. The 2D profile is shown together with a 1D line-scan through the beam center ($x = 0$), with the line-scan position marked in the 2D profile (white dashed line). The orange line in the 1D profile identifies the data used to fit the parabola at the beam center (black dashed line), whose curvature provides an estimation for the parameter α_0 from Eq. (24). The intensity is normalized such that the integrated 2D profile leads to a total power of 1 mW.

camera, we take a reference image without light, which is subtracted from the image with light in order to obtain the final picture. Figure 8 shows the resulting 2D profile, where the pixel illumination has been normalized such that the integrated signal provides a total power $P = 1 \text{ mW}$. In order to determine the beam curvature in the parabolic approximation (cf. Sec. II A), we consider the 1D intensity profile along a vertical line-scan passing through the beam center ($x = 0$), i.e. along the same direction as we observe the corresponding cloud shaping in the dark-state measurements. A parabolic function $I = \frac{1}{2}\alpha_0 P y^2$ is fitted to the 1D profile near the vortex center, resulting in $\alpha_0 = 1.2 \cdot 10^5 \text{ cm}^{-4}$.

Appendix B: Saturation intensity

Here, we estimate the saturation intensity for the $|5S_{1/2}, F = 2\rangle \rightarrow |5P_{3/2}, F' = 3\rangle$ transition, driven in the *dynamic scheme*, and the interval of possible saturation intensities for the $|5S_{1/2}, F = 2\rangle \rightarrow |5P_{3/2}, F' = 2\rangle$ transition, driven in the *dark-state scheme* to pump the atoms to the $|5S_{1/2}, F = 1\rangle$ state.

In general, the saturation intensity is inversely proportional to the transition strength, which depends on the coupling between the light polarization and the atomic dipole moment. As in the experiment, we consider a vortex beam with purely radial polarization (cf. Fig. 1b) propagating along the z axis. With the MOT magnetic field being turned off during the shaping pulse, we choose the quantization axis to point along the shaping beam di-

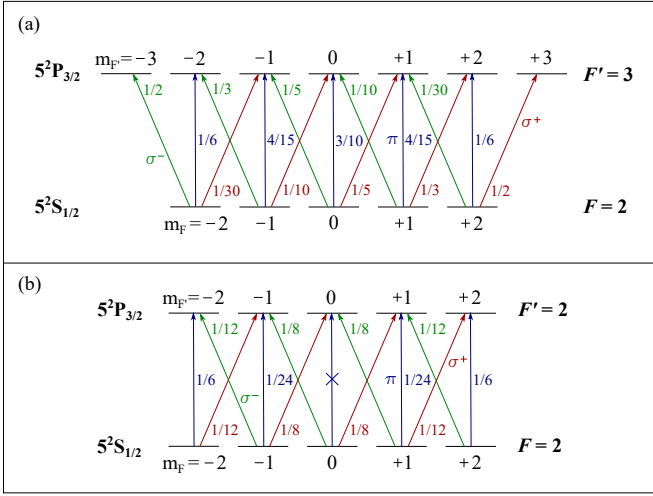


FIG. 9. Level Scheme for the (a) ^{87}Rb $|5^2S_{1/2}, F=2\rangle \rightarrow |5^2P_{3/2}, F'=3\rangle$ and (b) $|5^2S_{1/2}, F=2\rangle \rightarrow |5^2P_{3/2}, F'=2\rangle$ hyperfine transitions. Magnetic sub-levels are denoted by their respective $m_F, m_{F'}$ quantum numbers. Possible σ^+ , σ^- and π transitions are shown in red, green and blue, respectively, together with their relative excitation probabilities expressed as multiples of $P_{D_2} = |\langle J=1/2 || er || J'=3/2 \rangle|^2$ [32]. All other excitation probabilities are zero.

rection. At the position of each individual atom, the linear beam polarization is then oriented orthogonal to the quantization axis, driving σ^+ and σ^- transitions at half the beam power each. Figure 9 shows a schematic of the atomic sub-levels for the given ground and excited states, together with the possible transitions driven by the shaping light and the relative excitation probabilities, which are expressed as multiples of the absolute square of the reduced transition dipole matrix element for the D_2 line ($P_{D_2} = |\langle J=1/2 || er || J'=3/2 \rangle|^2$ [32]).

The coupling strength for an $|F\rangle \rightarrow |F'\rangle$ transition depends in general on the initial population distribution among the magnetic sub-levels, such that we can express the average coupling between the levels in terms of an average transition dipole moment, defined as

$$|\bar{d}_i|^2 = \langle F | d | F' \rangle_i^2 \quad (\text{B1})$$

$$= \sum_{m_F, m_{F'}, q} |\langle F m_F | er_q | F' m_{F'} \rangle|^2 P_{m_F}^i P_q. \quad (\text{B2})$$

Here, the first term in the summation is the excitation probability for the $|F, m_F\rangle \rightarrow |F', m_{F'}\rangle$ transition, with q referring to the angular momentum carried by the photon, ($q = \pm 1$ for σ^\mp and $q = 0$ for π transitions). With P_q we indicate the beam power distribution between the different types of transitions, which in our case are $P_1 = P_{-1} = 1/2$ and $P_0 = 0$. Finally, $P_{m_F}^i$ refers to the initial population distribution among the m_F sub-levels of the ground state.

To determine the saturation intensity for a specific transition and initial distribution, it is useful to express it in terms of a reference value $I_{\text{sat,ref}}$. Due to the in-

verse relationship between the saturation intensity and the dipole moment, the following expression holds

$$\frac{I_{\text{sat},i}}{I_{\text{sat,ref}}} = \frac{|\bar{d}_{\text{ref}}|^2}{|\bar{d}_i|^2}. \quad (\text{B3})$$

As a reference we consider the $|F=2, m_F=2\rangle \rightarrow |F'=3, m_{F'}=3\rangle$ cycling transition under σ^+ polarized light, for which $I_{\text{sat,ref}} = 1.67 \text{ mW cm}^{-2}$ [32]. In this case, the transition dipole moment $|\bar{d}_{\text{ref}}|^2$ is equal to the excitation probability between the given states and can be conveniently expressed as multiple of P_{D_2} , resulting in $1/2 P_{D_2}$ [32].

We now want estimate the saturation intensity of the $|5S_{1/2}, F=2\rangle \rightarrow |5P_{3/2}, F'=3\rangle$ transition, which is driven in the *dynamic scheme*. In this case, the shaping process occurs over multiple successive absorption-emission cycles, such that we can consider the population distribution as the one in the steady state. Solving the corresponding rate equations results in $P_{m_F=\pm 2} = 0.3638$, $P_{m_F=\pm 1} = 0.0924$, $P_{m_F=0} = 0.0876$ in our σ^+/σ^- pumping scheme. Following Eq. (B1) and summing over all σ^\pm transitions shown in Fig. 9a, we obtain $I_{\text{sat}} = 3.3 \text{ mW cm}^{-2}$ independent of the initial sub-level distribution.

In order to determine limiting values for the saturation intensity of the $|5S_{1/2}, F=2\rangle \rightarrow |5P_{3/2}, F'=2\rangle$ transition for the *dark-state scheme*, we consider two conditions for the atomic spin, namely a completely unpolarized- or polarized state, and calculate the corresponding average of the squared transition dipole moments. In the first case, the atomic population is equally distributed among the five ground state sub-levels, hence $P_{m_F}^i = 1/5$. Following Eq. (B1) and summing over all σ^\pm transitions shown in Fig. 9b, we then obtain $|\bar{d}|^2 = 1/12 P_{D_2}$. From Eq. (B3), this results in $I_{\text{sat}} = 10 \text{ mW cm}^{-2}$. In the second case of a fully polarized state, we assume the whole atomic population to be in the $m_F = +2$ sub-level, meaning that $P_{m_F=2} = 1$ is the only non-zero contribution. Again, following Eq. (B1), we find $|\bar{d}|^2 = 1/24 P_{D_2}$, leading to $I_{\text{sat}} = 20 \text{ mW cm}^{-2}$. Depending on the specific initial state population, the saturation intensity is thus expected to be between $10 - 20 \text{ mW cm}^{-2}$. While the initial state population is not easily accessible in a magneto-optical trap, it also changes during the optical pumping. In our σ^+/σ^- pumping scheme, a steady-state population distribution is reached after sufficient absorption-emission cycles, with $P_{m_F=\pm 2} = 0.2710$, $P_{m_F=\pm 1} = 0.1369$ and $P_{m_F=0} = 0.1843$, resulting in a saturation intensity of $11.3 \frac{\text{mW}}{\text{cm}^2}$. However, this value cannot be taken as a reference in our case, as the atoms will be pumped to the $|5^2S_{1/2}, F=1\rangle$ dark state before this distribution is reached.

-
- [1] C. Gross and I. Bloch, *Science* **357**, 995 (2017).
- [2] A. Browaeys and T. Lahaye, *Nature Physics* **16**, 132 (2020).
- [3] L. Henriët, L. Beguin, A. Signoles, T. Lahaye, A. Browaeys, G.-O. Reymond, and C. Jurczak, *Quantum* **4**, 327 (2020).
- [4] A. M. Kaufman and K.-K. Ni, *Nature Physics* **17**, 1324 (2021).
- [5] H. Metcalf and P. van der Straten, *Physics reports* **244**, 203 (1994).
- [6] R. Folman, P. Krüger, J. Schmiedmayer, J. Denschlag, and C. Henkel, in *Advances in atomic, molecular, and optical physics*, Vol. 48 (Elsevier, 2002) pp. 263–356.
- [7] J. Fortágh and C. Zimmermann, *Rev. Mod. Phys.* **79**, 235 (2007).
- [8] J. Reichel and V. Vuletic, *Atom chips* (John Wiley & Sons, 2011).
- [9] R. Grimm, M. Weidemüller, and Y. B. Ovchinnikov, in *Advances in atomic, molecular, and optical physics*, Vol. 42 (Elsevier, 2000) pp. 95–170.
- [10] P. Jessen and I. Deutsch, *Advances in Atomic, Molecular, and Optical Physics* **37**, 95 (1996).
- [11] C. Muldoon, L. Brandt, J. Dong, D. Stuart, E. Brainis, M. Himsworth, and A. Kuhn, *New Journal of Physics* **14**, 073051 (2012).
- [12] M. Endres, H. Bernien, A. Keesling, H. Levine, E. R. Anschuetz, A. Krajenbrink, C. Senko, V. Vuletic, M. Greiner, and M. D. Lukin, *Science* **354**, 1024 (2016).
- [13] G. Roati, D. Chiara, L. Fallani, M. Fattori, C. Fort, M. Zaccanti, G. Modugno, M. Modugno, and M. Inguscio, *Nature* **453**, 895 (2008).
- [14] J. Billy, V. Josse, Z. Zuo, A. Bernard, B. Hambrecht, P. Lugan, D. Cl, L. Sanchez-Palencia, P. Bouyer, and A. Aspect, *Nature* **453**, 891 (2008).
- [15] N. Cooper, J. Dalibard, and I. Spielman, *Reviews of modern physics* **91**, 015005 (2019).
- [16] M. Greiner, O. Mandel, T. Esslinger, T. W. Hänsch, and I. Bloch, *Nature* **415**, 39 (2002).
- [17] K. Sueda, G. Miyaji, N. Miyanaga, and M. Nakatsuka, *Opt. Express* **12**, 3548 (2004).
- [18] N. R. Heckenberg, R. McDuff, C. P. Smith, and A. G. White, *Opt. Lett.* **17**, 221 (1992).
- [19] C.-H. Yang, Y.-D. Chen, S.-T. Wu, and A. Y.-G. Fuh, *Scientific reports* **6**, 31546 (2016).
- [20] J. W. Kim and W. Clarkson, *Optics Communications* **296**, 109–112 (2013).
- [21] S. C. McEldowney, D. M. Shemo, and R. A. Chipman, *Opt. Express* **16**, 7295 (2008).
- [22] S. Fu and C. Gao, *Optical vortex beams* (Springer, 2023).
- [23] R. C. Jones, *Journal of the Optical Society of America* **31**, 488 (1941).
- [24] E. Hecht, *Optik* (Walter de Gruyter GmbH & Co KG, 2023).
- [25] M. Born and E. Wolf, *Principles of Optics*, 7th ed. (Cambridge University Press, 2020).
- [26] M. Beijersbergen, R. Coerwinkel, M. Kristensen, and J. Woerdman, *Optics Communications* **112**, 321 (1994).
- [27] S. A. Collins, *J. Opt. Soc. Am.* **60**, 1168 (1970).
- [28] A. Mawardi, S. Hild, A. Widera, and D. Meschede, *Opt. Express* **19**, 21205 (2011).
- [29] I. S. Gradshteyn and I. M. Ryzhik, *Table of integrals, series, and products*, seventh ed. (Elsevier/Academic Press, Amsterdam, 2007) pp. xlviii+1171, translated from the Russian, Translation edited and with a preface by Alan Jeffrey and Daniel Zwillinger.
- [30] F. W. Olver, D. W. Lozier, R. F. Boisvert, and C. W. Clark, *NIST Handbook of Mathematical Functions*, 1st ed. (Cambridge University Press, USA, 2010).
- [31] W. Ketterle, D. S. Durfee, and D. Stamper-Kurn, in *Bose-Einstein condensation in atomic gases* (IOS Press, 1999) pp. 67–176.
- [32] D. A. Steck, Rubidium 87 D Line Data, available online at <http://steck.us/alkalidata> (revision 2.3.3, 28 May 2024).